ELSEVIER

Contents lists available at ScienceDirect

Electrochimica Acta

journal homepage: www.journals.elsevier.com/electrochimica-acta





Sr₂Fe_{2–X}Mo_XO₆ double perovskites as electrocatalysts for oxidative dehydrogenation of ethane: Effect of B-site stoichiometry

Jaesung Kim^a, Matthew Ferree^a, Seval Gunduz^a, Anne C. Co^b, Umit S. Ozkan^{a,*}

- a William G. Lowrie Department of Chemical and Biomolecular Engineering. The Ohio State University, Columbus, Ohio, 43210, United States
- b Department of Chemistry and Biochemistry, The Ohio State University, Columbus, Ohio, 43210, United States

ARTICLE INFO

Keywords:
Ethane dehydrogenation
Olefin production
Solid oxide electrocatalytic cell

ABSTRACT

The oxidative dehydrogenation of ethane (ODHE) was investigated using a solid oxide electrocatalytic cell with $Sr_2Fe_{2-X}Mo_XO_{6-\delta}$ (SFM) double perovskite as the anode electrocatalyst. As shown in the XRD patterns, SFM perovskites maintained their cubic structure upon modifying the B-site ratios of Mo and Fe. Increasing the Mo content of the perovskite structure resulted in a lower water signal intensity at low temperatures in TPR profiles, indicative of moderate oxygen transport through the perovskite structure. Because Mo–O bonds are stronger than Fe–O bonds, the electrical conductivity of SFM perovskites decreased with increasing Mo content. When operated at 100 mA cm⁻², ODHE activity improved four times compared to open circuit voltage, resulting in 16.1% conversion of C_2H_6 and 83.1% selectivity to C_2H_4 . It has been demonstrated that oxygen ions provided by perovskite lattices were the key species involved in activating C_2H_6 based on the *in-situ* DRIFTS experiments. The SFM perovskite with higher Mo content showed the highest conversion and selectivity due moderate oxygen ion mobility and fast desorption of C_2H_4 .

1. Introduction

Ethylene (C_2H_4) is a crucial building block in in the petrochemical industry, with steam cracking being the most dominant method for its production [1]. However, steam cracking has several shortcomings, including thermal constraints, high operating temperatures, and high energy consumption. The abundance of shale gas reserves has made ethane an attractive alternative feedstock for C_2H_4 production. In this context, oxidative dehydrogenation of ethane (ODHE) has emerged as a promising alternative to conventional production methods [2,3].

ODHE is an exothermic reaction that occurs at low temperatures (400–700°C), allowing for energy efficient operation [4,5]. The reaction is represented by eq. 1:

$$C_2H_6 + \frac{1}{2}O_2 \rightarrow C_2H_4 + H_2O$$
 (1)

ODHE produces H_2O rather than H_2 , eliminating the thermodynamic limitation. Moreover, H_2O is easier to separate from the product stream than H_2 . There are many alternatives to run oxidative dehydrogenation reactions, the most common of which requires molecular oxygen to act as the oxidant in a packed-bed reactor. However, in the presence of molecular oxygen, complete oxidation of the olefin product or even the

alkane itself remains a challenge in packed-bed reactors [6]. This issue reduces overall olefin selectivity, thereby limiting the effectiveness of ODHE.

Recent advances in electrocatalytic conversion of alkanes using solid oxide electrocatalytic cells (SOECs) have attracted significant attention [6–9]. In SOECs, the amount of oxygen involved in the oxidative dehydrogenation reaction can be controlled by the applied potential, which regulates the amount of oxygen ions available on the surface of anode catalyst. This approach allows for the inhibition of both the coke formation and the complete oxidation of alkanes or the olefins. The anode and cathode half-cell reactions are as follows:

Anode:
$$C_2H_6 + O^{2-} \rightarrow C_2H_4 + H_2O + 2e^-$$
 (2)

Cathode :
$$\frac{1}{2}O_2 + 2e^- \rightarrow O^{2-}$$
 (3)

SOECs use mixed electronic and ionic conducting (MIEC) ceramics, such as perovskite oxides and double perovskite oxides, as electrode materials due to their high redox stability [10,11]. As perovskites have ABO $_3$ or A $_2$ BB'O $_6$ structure, they can be formed by combining a variety of elements, which can be tuned to improve their ionic conductivity, electronic conductivity, and electrocatalytic activity. Doping strategies

E-mail address: Ozkan.1@osu.edu (U.S. Ozkan).

^{*} Corresponding Author

in the A and B sites have also been shown to influence the characteristics of the materials, including conductivity, stability, and activity. Double perovskites containing iron and molybdenum ($Sr_2Fe_{2-X}Mo_XO_{6-\delta}$) have been shown to exhibit high electron transport due to their mixed valence characteristic of both molybdenum ($Mo^{5+/6+}$) and iron ($F^{e2+/3+/4+}$) ions [12].

This study examines the electrocatalytic activity of $\rm Sr_2Fe_{2-X}Mo_XO_{6-\delta}$ (SFMx, x=0.35, 0.40, 0.45) double perovskite with varying B-site stoichiometry as an anode in a solid oxide electrocatalytic cell for ODHE. The material properties of SFM double perovskites with different ratios of Mo to Fe were characterized using various surface and bulk characterization techniques. The findings of this study could lead to the development of more efficient and sustainable methods for the production of ethylene.

2. Experimental

2.1. Preparation of catalysts

 $Sr_2Fe_{2-X}Mo_XO_{6-\delta}$ double perovskite (SFM(X) (X=45, 40, 35)) was synthesized via a sol-gel method with different stoichiometries. (NH₄)₆Mo₇O₂₄·4H₂O, Sr(NO₃)₂ and Fe(NO₃)₃·9H₂O were dissolved in 100 mL deionized water. Citric acid was added to the solution at room temperature in an equimolar ratio to the total metal ions. The solution was heated to 80 °C until a gel was formed. The gel was dried at 150 °C overnight and calcined at 1100 °C.

2.2. Characterization

X-ray diffraction patterns of the catalysts were examined with a Bruker D8 Lead X-ray powder diffractometer using a Cu K α source. The Crystallographic Open Database (COD) was used to identify phases [13]. XRD patterns were analyzed using General Structure Analysis System-2 (GSAS-2) software to calculate Miller indices by Rietveld refinement [14]. Images of crystal structures were generated using VESTA [15].

The effluent from temperature-programmed reduction (TPR) was analyzed using a MKS Cirrus mass spectrometer by monitoring H_2O signal (m/z=18). 30 ccm of 5% H_2/N_2 was introduced into the reactor, and it was heated from room temperature to 1000 $^{\circ}C$ at a rate of 10 $^{\circ}C$ min $^{-1}$.

To measure the electrical conductivity, the powder was compressed in a hydraulic press, then sintered at 1300° C for 5 h. Four gold wires were connected to four points on the pellet using gold paste. Current was applied to the two leads using the Keithley 6220 current source. A Keithley 6182 sensitive nanovoltmeter was used to measure the voltage on the two leads.

X-ray photoelectron Spectroscopy (XPS) was utilized to explore the surface elemental oxidation state and composition using a Thermo-Scientific Nexsa X-ray Photoelectron Spectrometer with a hemispherical analyzer and monochromatic Al K α source. The SFM samples were mounted on the standard XPS sample holder using a Cu spring clip and held under vacuum for more than 30 min. The base pressure of the analysis chamber during the experiment was $\sim\!1.7\times10^{-7}$ mbar. A flood gun was employed for surface charge neutralization.

Diffusion reflectance infrared Fourier transform spectroscopy (DRIFTS) data was collected using a Thermoelectron Nicolet 6700 FTIR equipped with an MCT detector. In order to dilute samples, catalyst powders were mixed with potassium bromide (KBr) at a 1:10 ratio. Pretreatment with helium at 450°C was performed on SFM perovskites. *In-situ* DRIFTS spectra were recorded under 10% C_2H_6 /He and 99.99% or C_2H_4 at 450°C. TPD-DRIFTS spectra were collected under helium flow of 30 ccm after SFM perovskites were subjected to 99.99% C_2H_4 for 5 min at 50 °C.

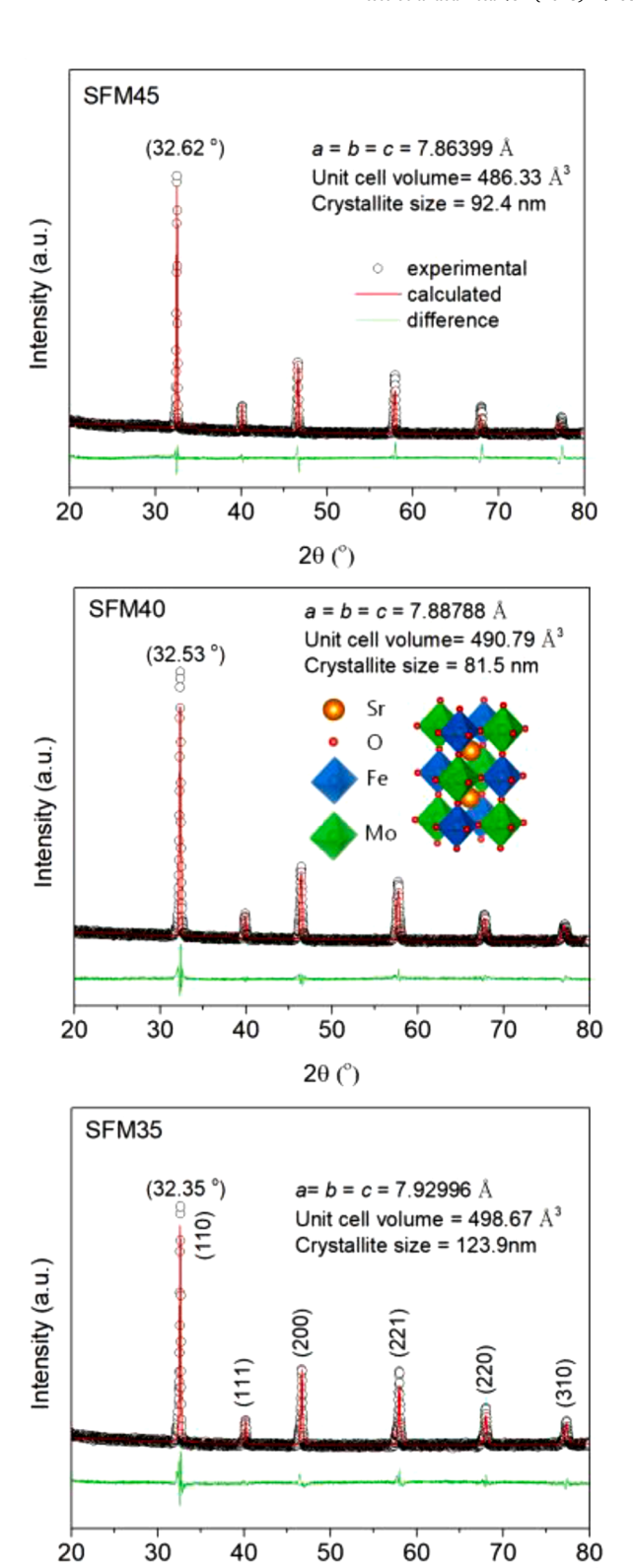


Fig. 1. XRD patterns of SFM45, SFM40, and SFM35.

2θ (°)

2.3. Evaluation of electrocatalytic performance

An electrocatalytic button cell was made by screen-printing electrode materials on a commercial Yttria-stabilized zirconia (YSZ) electrolyte (25 mm diameter, $125~\mu$ thickness, Nextech Materials). The

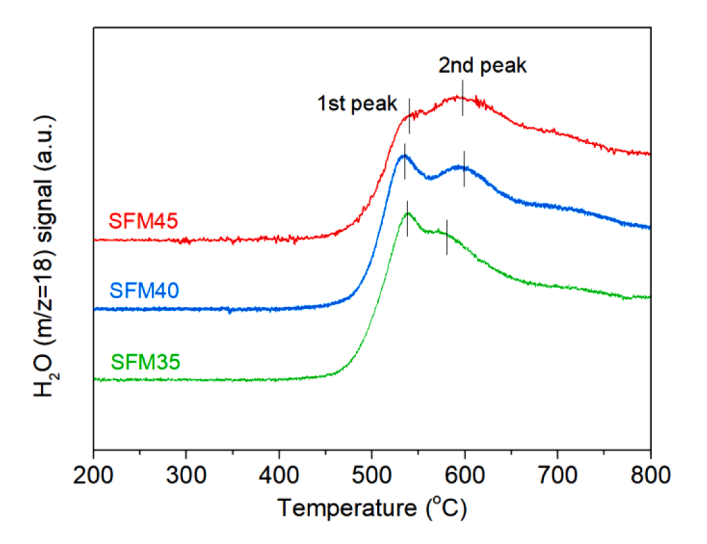


Fig. 2. Temperature-programmed reduction under 30 ccm of 5% H₂/N₂ flow.

anode side of the cells was interlayered with gadolinium doped ceria (GDC; Nextech Materials) that was sintered at 1400°C for 2 h under air flow. In order to make the SFM anode layer, GDC (40 wt%) was mixed with SFM and printed on the GDC to provide an electrode surface area of 0.72 cm². For the cathode, commercial (La_{0.80}Sr_{0.20})_{0.95}MnO₃-(Y2O3)0.08(ZrO2)0.92 (LSM-YSZ; Nextech Materials) was used, and the cell was sintered at 1200°C under air for 2 h. Silver wire and paste were used to attach silver mesh to the electrodes. For electrocatalytic performance testing, 15 ccm of 10% C₂H₆/He was flowed into the anode and the cathode side was left open to air. Gas products were analyzed using a Shimadzu 2014 on-line gas chromatograph with a pulse discharge helium ionization detector (PDHID) and flame ionization detectors (FID). Electrochemical impedance spectra (EIS) were acquired in the frequency range of 1 MHz to 10 mHz. Polarization resistance was calculated using Zsim software based on the fitted EIS [16]. The ethane conversion was calculated based on the ethane concentration difference between the feed and the effluent,

$$X_{C_2H_6} = \frac{y_{C_2H_6}^{in} - y_{C_2H_6}^{out}}{y_{C_2H_6}^{in}} \times 100\%$$
 (4)

where $y^{in}_{C_2H_6}$ and $y^{out}_{C_2H_6}$ are the ethane mole fractions in the feed and the effluent stream, respectively. The selectivity for the species j was calculated as

$$S_j = \frac{n_j y_j}{\sum n_i y_i} \times 100\% \tag{5}$$

where n is the number of carbon atoms in the product molecule.

3. Results and discussion

3.1. Structural analysis

X-ray diffraction was used to analyze the structure of the synthesized double perovskites at room temperature. Fig. 1 shows the XRD patterns along with Rietveld refinement results. SFM perovskites were found to have a cubic structure with a space group of Fm-3m. As the Mo content was increased, no impurity phases were observed. The structural equivalence of the synthesized SMF double perovskites to $Sr_2Fe_{1.5}$. $Mo_{0.5}O_6$ (COD: 1531825) was confirmed by Rietveld refinement [13]. The analysis further revealed that the principal peak of the (110) plane shifted to lower degrees as the Mo to Fe ratio decreased. The shift resulted in an increase in the unit cell volume, as displayed in Fig. 1. The smaller radius of molybdenum ions (Mo^{5+} : 0.610 Å, Mo^{6+} : 0.59 Å) compared to that of the iron ions (Fe^{3+} : 0.645 Å, Fe^{4+} : 0.585 Å) is likely

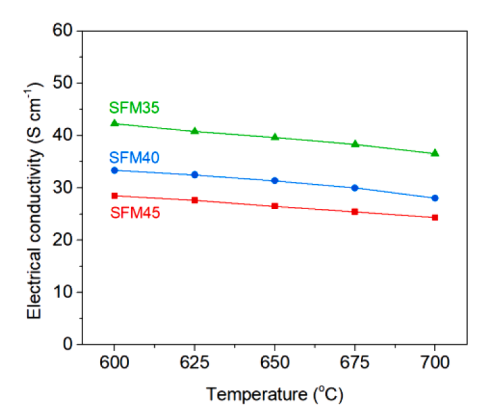


Fig. 3. Electrical conductivity of SFM perovskites at different temperatures.

to be responsible for this increase [17]. The crystallite size of SFM perovskites was calculated using Scherrer equation [18] by assuming a spherical particle shape. The equation is given as follows:

$$\beta_L = \frac{K\lambda}{Lcos(\theta)} \tag{6}$$

Where K is a dimensionless shape factor of 0.9, β_L is the peak broadening (FWHM) in radians, λ is the wavelength of Cu-K α radiation (0.15406 nm), and L is the crystallite size. The calculated L values for the SFM perovskites were found to range from 92.4 nm to 123.9 nm.

3.2. Temperature-programmed reduction (TPR) analysis

Catalyst reducibility is a crucial parameter that governs the conversion of ethane and selectivity to etylene. It has been reported that catalysts with higher reducibility exhibit an increased conversion of C_2H_6 , whereas catalysts with lower reducibility demonstrate an enhanced selectivity for C_2H_4 [19]. The reduction behavior of a catalyst can be evaluated effectively through the H_2 -temperature programmed reduction (TPR) method.

TPR profiles of SFM perovskites in 5% H₂/N₂ are provided in Fig. 2 to investigate their reducibility. The TPR profiles were obtained by measuring the evolution of H₂O (m/z=18) as a function of temperature, up to 1000 °C. The first peak, observed at around 530 °C, corresponds to the reduction of Fe ions (Fe⁴⁺ \rightarrow Fe³⁺ \rightarrow Fe²⁺). The temperature at which the first peak occurs remains relatively unchanged, ranging from 535-540 °C in SFM perovskites with varying levels of Mo content. Conversely, the second peak, attributed to the reduction of Mo ions (Mo $^{6+}{\rightarrow} \text{Mo}^{5+}$), displays a noticeable increase in temperature from 578 $^{\circ}\text{C}$ to 597 $^{\circ}\text{C}$ as the Mo content in SFM perovskites increases [20]. This result suggests that SFM perovskites with higher Mo content exhibit lower reducibility and moderate oxygen ionic conductivity. It is worth mentioning that a greater peak intensity was observed for Mo reduction in SFM45 compared to Fe reduction, and the peak intensity of Fe increased as the Mo content decreased. The temperature at which each ion is reduced is an essential factor affecting catalyst reducibility. The SFM perovskites with higher Mo to Fe ratios exhibited lower oxygen mobility through the lattice, as Mo ions are reduced at higher temperatures than Fe ions. Therefore, the reducibility of SFM perovskites can be tuned by adjusting the ratio of Mo to Fe in the catalyst.

3.3. Electrical conductivity

The electrical conductivity of SFM perovskites was studied as a function of temperature in the range of 600–700 °C under air, and the results are presented in Fig. 3. Among the synthesized SFM perovskites, SFM45 perovskite exhibited the lowest conductivity ranging from 24.3 S cm⁻¹ to 28.5 S cm⁻¹, which is comparable to value reported for $Sr_2Fe_{1.5}Mo_{0.5}O_6$ perovskite in the literature [21]. Interestingly, it was

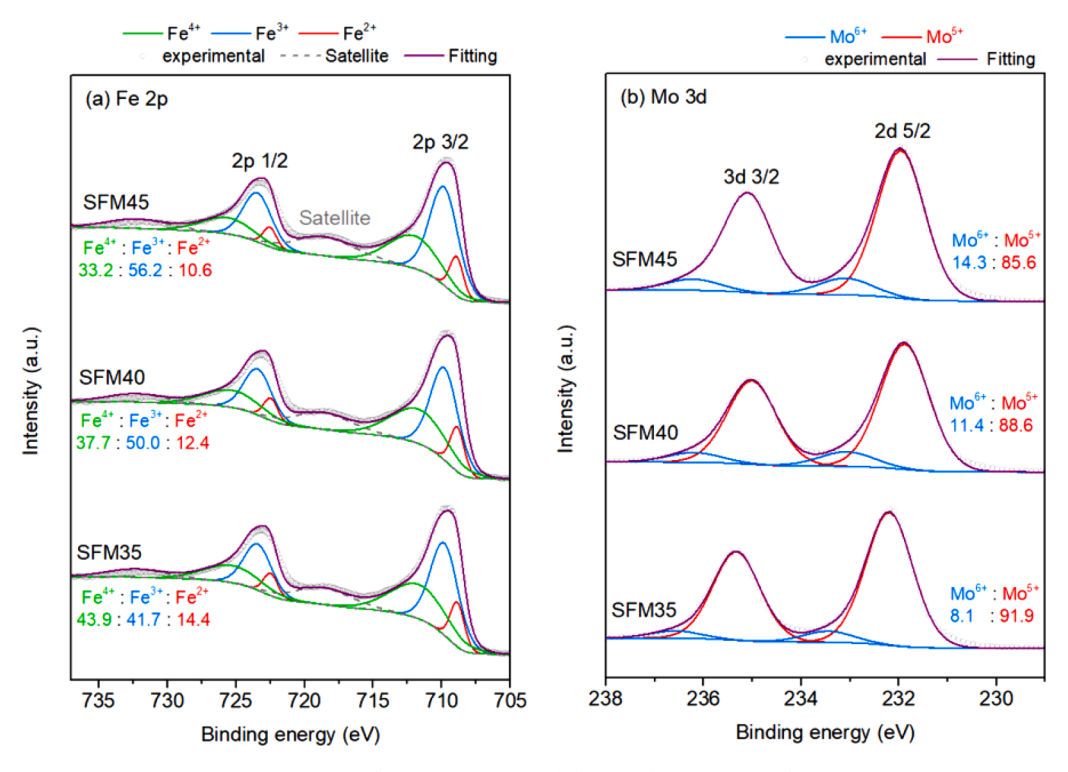


Fig. 4. XPS analysis on (a) Fe 2p and (b) Mo 3d on SFM perovskites.

found that the electrical conductivity of SFM perovskites increased with decreasing Mo composition, resulting in a range of $28.0-33.3~\rm S~cm^{-1}$ for SFM40 and $36.6-42.3~\rm S~cm^{-1}$ for SFM35.

The increase in conductivity with decreasing Mo composition can be attributed to the substitution of Mo ions by Fe ions. As the electrical conductivity of SFM perovskites is based on a small polaron conduction mechanism, ${\rm Mo^{5+}/Mo^{6+}}$ or ${\rm Fe^{3+}/Fe^{4+}}$ ion pairs must serve as charge carriers for electrons within the crystal [22]. The lower reducibility of Mo compared to Fe results in the formation of oxygen vacancies in the following order: Fe–O–Fe > Fe–O–Mo > Mo–O-Mo. Consequently, SFM perovskites with a higher ratio of Mo to Fe exhibit lower electrical conductivity.

Moreover, the electrical conductivity of SFM perovskites was

observed to decline with increasing temperature in the measured temperature range. This behavior can be attributed to electroneutrality, where an increase in the concentration of oxygen vacancy at high temperature results in a decrease in the concentration of ${\rm Mo}^{5+/6+}$ and ${\rm Fe}^{3+/4+}$ ion pairs, leading to a reduction in the electrical conductivity of p-type conductive materials.

3.4. X-ray photoelectron spectroscopy analysis

The electrocatalytic performance of SFM perovskites is strongly influenced by the oxidation state and atomic concentration of their surface elements. To investigate these properties, X-ray photoelectron spectroscopy (XPS) was used to analyze SFM perovskite samples. The

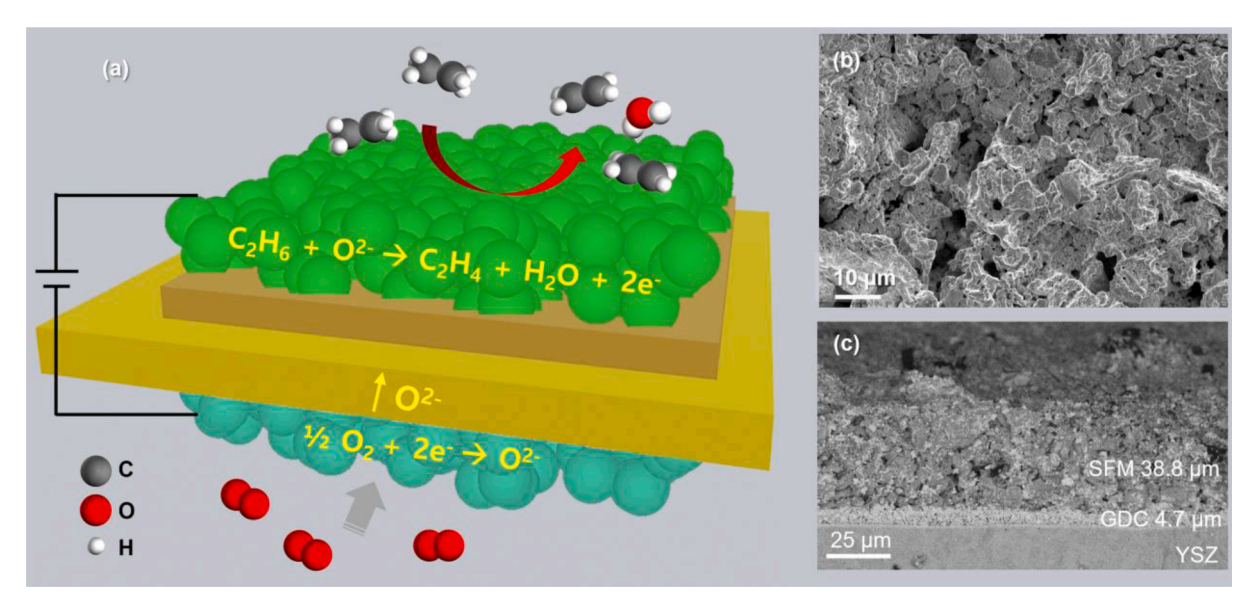


Fig. 5. Schematic illustration of SFM cells and SEM images of the button cells.

J. Kim et al. Electrochimica Acta 461 (2023) 142633

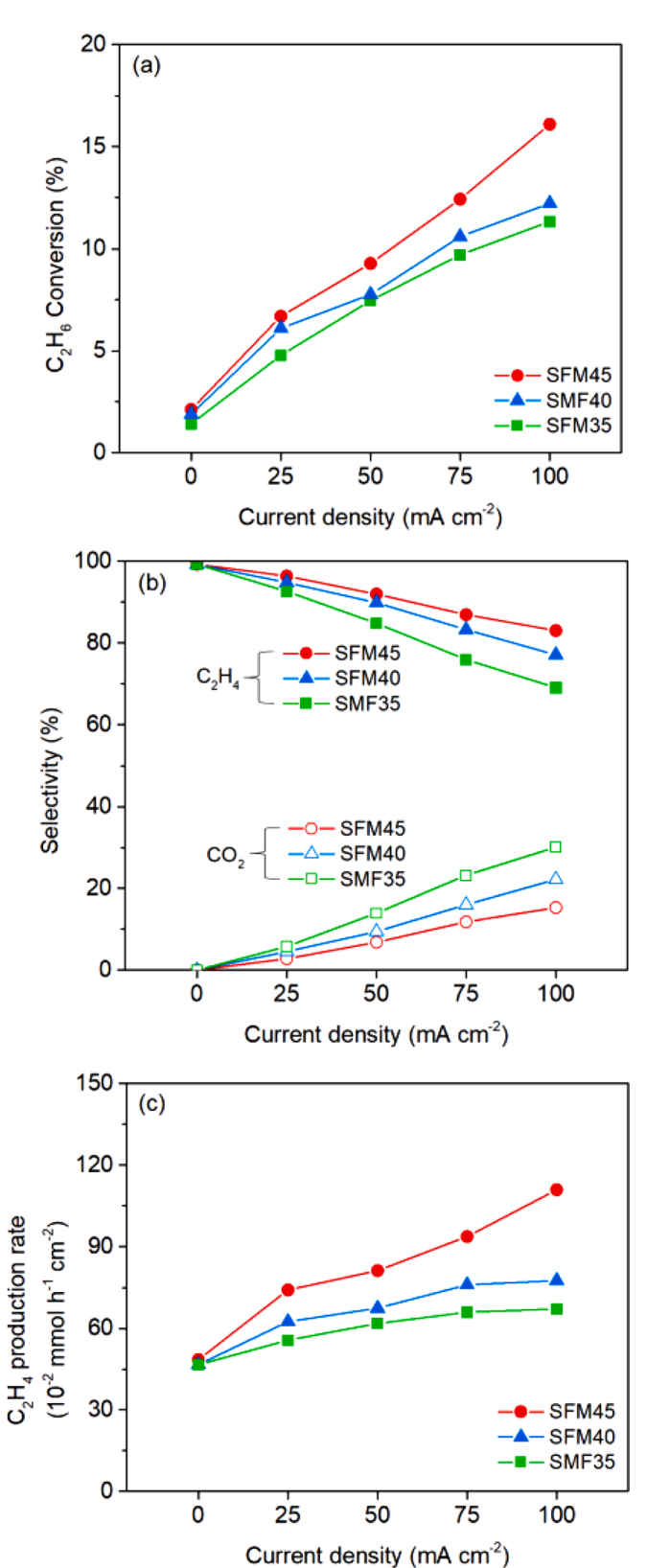


Fig. 6. Electrocatalytic ODHE on SFM perovskites at 680 °C.

XPS spectra in the Fe 2p and Mo 3d regions were plotted as a function of binding energy and are shown in Fig. 4. The atomic composition of the samples was also calculated from the XPS spectra.

An analysis of the binding energies of the Fe $2p_{3/2}$ peak and the satellite peak has been proposed as a means of determining the presence

of Fe^{2+} and Fe^{3+} ions [23].

$$\Delta Fe2p_{3/2} = BE \left[Sat \left(Fe2p_{3/2} \right) \right] - BE \left[Fe2p_{3/2} \right]$$
 (7)

The study notes that compounds containing Fe³⁺ ions typically exhibit a difference of approximately 8 eV of difference between the Fe 2p_{3/2} peak and the satellite peak, whereas compounds of the Fe²⁺ ions exhibit a difference of 4.3-5.65 eV. The observed differences in the binding energies on SFM45, SFM40, and SFM35 were estimated to be 8.56 eV, 8.62 eV, and 8.65, respectively, indicating prevalence of Fe³⁺ species on the surface. Moreover, deconvolution of the Fe 2p peaks revealed three constituents corresponding to Fe²⁺, Fe³⁺ and Fe⁴⁺ ions [24]. Fe²⁺ peaks were observed at 708.8 eV and 722.4 eV for Fe $2p_{3/2}$ and Fe $2p_{5/2}$, respectively [25]. For Fe³⁺ species, the components that have binding energies of around 710.0 eV and 723.6 eV correspond to Fe $2p_{3/2}$ and Fe $2p_{1/2}$, respectively [26,27]. 713 eV and 726.6 eV are the peaks that can be attributed to Fe^{4+} . The presence of $Fe^{4+/3+/2+}$ redox couples in perovskites is known to be critical, as they function as p-type carriers of charge and enable electronic conductivity through the catalysts [28].

Fig. 4(b) illustrates the two asymmetrical peaks corresponding to the $3d_{5/2}$ and $3d_{3/2}$ states of Mo, which are split for all compositions. These peaks were fitted into two pairs of peaks and assigned to Mo^{6+} and Mo^{5+} states, respectively [29]. The concentration of Mo^{6+} in SFM perovskites decreases as the Mo stoichiometry decreases. Specifically, the Mo^{6+} concentration decreased from 14.3% in SFM45 to 8.1% in SFM35, indicating a decrease in the average oxidation state of Mo ions in SFM perovskites from 5.14 to 5.08. This study also observed a higher binding energy of Mo^{6+} ions in SFM35 (233.4 eV) compared to SFM45 (233.0 eV), and an increase in the binding energy of Mo^{5+} ions from 231.9 eV in SFM45 to 232.2 eV in SFM35. Previous reports have suggested that a higher content of Mo^{5+} ions in SFM double perovskites can improve their stability in reducing atmospheres [22].

3.5. Electrocatalytic performance for ODHE

The electrocatalytic performance of SFM perovskites for oxidative dehydrogenation of ethane (ODHE) was carried out at 680 °C. For this purpose, an SFM perovskite anode and LSM-YSZ cathode were employed as shown in Fig. 5(a). The cathode was exposed to air while 10% C₂H₆ was fed to the anode side. The morphology of the SFM45 electrode was analyzed using SEM, which revealed that the electrode material was well-densified vet retained porosity for effective mass transfer (Fig. 5 (b)). The cross-section of the button cell showed a GDC layer that was deposited between SFM electrode and YSZ electrolyte to prevent the formation of insulating phases resulting from the reaction between ferrite and YSZ, (Fig. 5(c)). The thickness of the GDC layer was estimated to be 4.7 µm, which is significantly thinner than the YSZ electrolyte (125 μm) and therefore expected to have minimal impact on the overall electrochemical performance. Moreover, the thickness of the electrode was estimated to be 38.8 µm, which is thick enough to provide catalytic activity.

The performance metrics of electrocatalytic ODHE on SFM perovskite anodes are shown in Fig. 6. Under open-circuit voltage (OCV), the highest conversion of C_2H_6 observed was 4.2% on the SFM45 catalyst and the selectivity of C_2H_4 was measured to be 99.2% for all three SFM catalysts, indicating that SFM perovskites are selectively active for nonoxidative dehydrogenation of ethane. When electricity was applied to the cells, the conversion of C_2H_6 substantially increased because of the supplied oxygen ions to the anode surface. The SFM45 cell achieved a four-fold improvement in conversion (16.1% at 100 mA cm $^{-2}$). Increasing the current density to 100 mA cm $^{-2}$ resulted in a decrease in the selectivity of C_2H_4 from 99.2% to 83.1%. However, C_2H_4 production increased from 53×10^{-2} mmol h $^{-1}$ cm $^{-2}$ to 111×10^{-2} mmol h $^{-1}$ cm $^{-2}$, an increase of 109%. It follows from this that the dehydrogenation of ethane to ethylene is an electrocatalytically activated reaction,

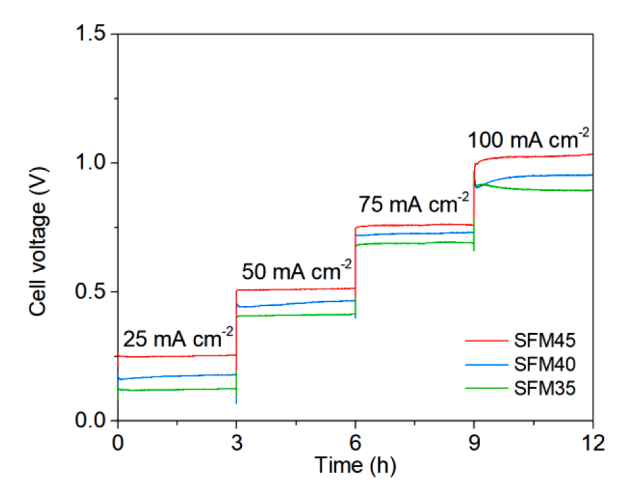


Fig. 7. Current-voltage relations on SFM perovskites for the electrocatalytic ODHE at 680 $^{\circ}\text{C}$ at different current densities.

indicating that oxygen ions supplied by bias are crucial for the ODHE reaction to take place. Among the three SFM perovskites synthesized, SFM45 was the most selective as well as reactive when it comes to producing C_2H_4 . The observed result can be attributed to the faster desorption of C_2H_4 on SFM perovskite with a higher Mo content. A faster olefin desorption can also lead to a faster catalytic active site turnover. Section 3.6 will discuss the desorption of C_2H_4 on SFM perovskites in

more detail. The current-voltage relationship is shown as a function of time at different current densities in Fig. 7. The SFM perovskites demonstrated stable cell voltages for 3 h at various current densities, which implies that they can be used as an anode for ODHE. Because of the lower electrical and ionic conductivity as demonstrated above, the SFM45 perovskite exhibited the highest cell voltage, consuming more electricity than SFM40 and SFM35.

The electrochemical impedance spectra (EIS) on the SFM perovskites were shown in Fig. 8 with polarization resistance. In Nyquist plots at high frequency, the intercept at X-axis was shifted to zero by subtracting the ohmic resistance (Z_b). The fit results were based on the equivalent circuit model, $R_S(R_{P1}Q_1)(R_{P2}Q_2)$ (Fig. 8a- inset), and are presented as solid lines. The total polarization resistance under OCV significantly higher than those under applied current, indicating that the ODHE reaction is electrocatalytically activated. According to Fig. 8(d), the polarization resistance at low frequency (R_{LF}), corresponding to the mass transfer at the interface between the surface of the SFM and the gas phase, decreased with the increase in the applied current density. This is because the supplied oxygen ions by bias facilitate the consumption of C₂H₆ at the interface, resulting in an increase in diffusion of C₂H₆ from the gas phase to the electrode surface. In contrast, it appears that the polarization resistance at high frequency (R_{HF}) is independent on the applied current (Fig. 8(d)). This may be explained by the fact that R_{HF} is mainly determined by the electrolyte, contact resistance at the interfaces between the electrode and the electrolyte, and the current collectors [30].

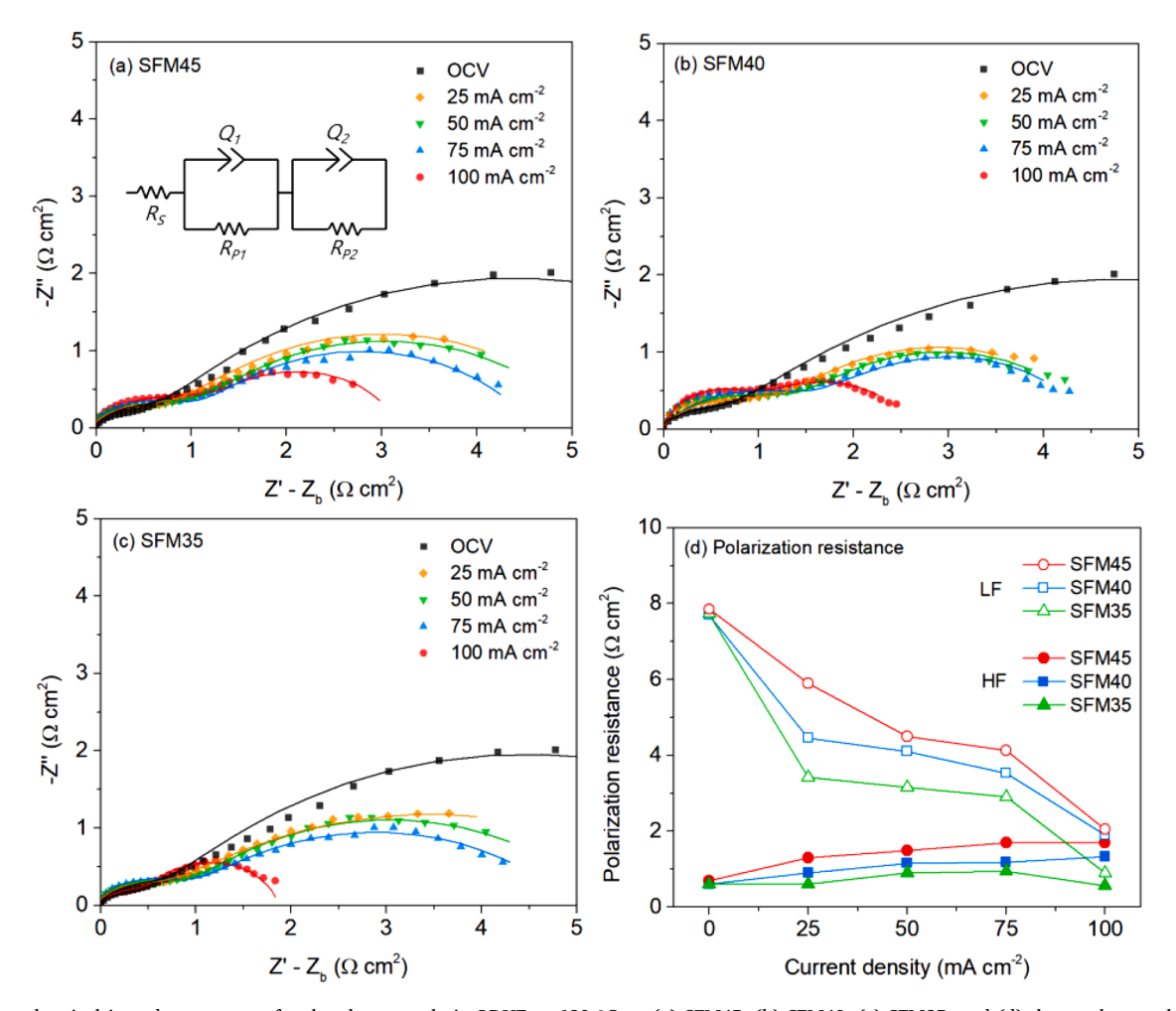


Fig. 8. Electrochemical impedance spectra for the electrocatalytic ODHE at 680 °C on (a) SFM45, (b) SFM40, (c) SFM35, and (d) the resultant polarization resistances at low (LF) and high frequency (HF). The equivalent circuit model is shown as an inset in (a).

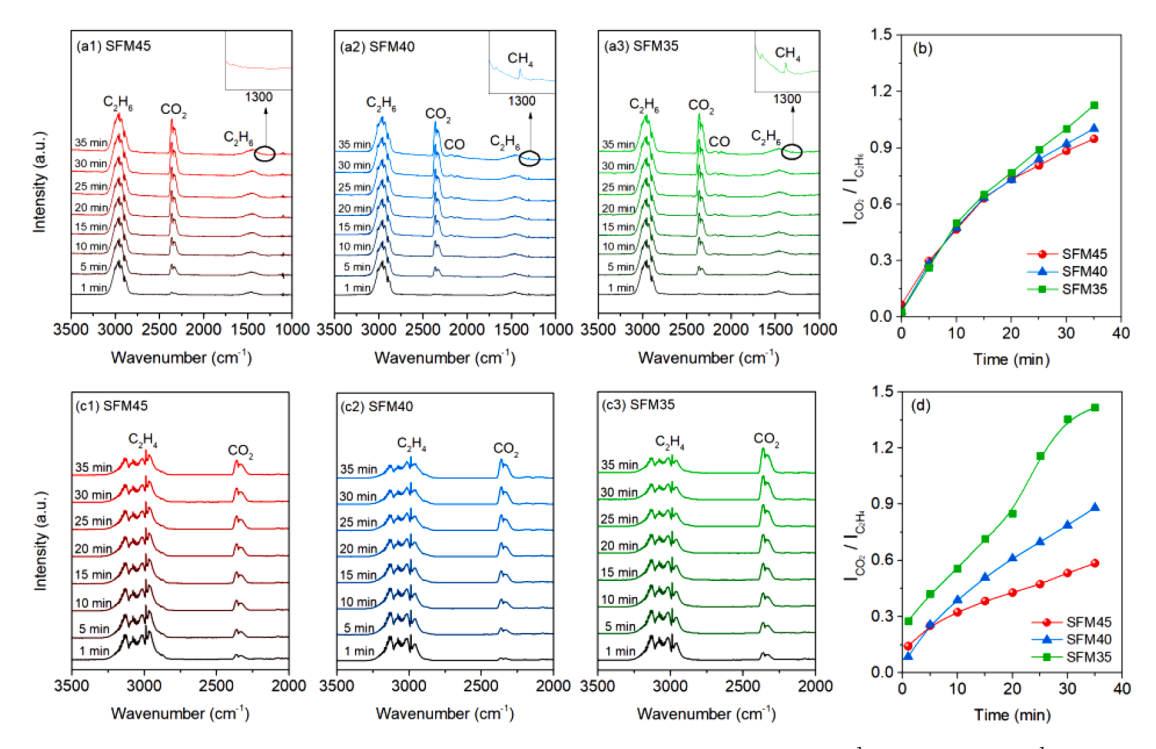


Fig. 9. (a) In-situ DRIFTS under C_2H_6 at 450 °C on SFM perovskites and (b) peak intensity ratio of CO_2 (2365 cm⁻¹) to C_2H_6 (2968 cm⁻¹), (c) In-situ DRIFTS under C_2H_4 at 400 °C on SFM perovskites and (d) peak intensity ratio of CO_2 (2365 cm⁻¹) to C_2H_4 (2988 cm⁻¹).

3.6. In-situ DRIFTS under C₂H₆ and C₂H₄

Interaction of the SFM perovskite surfaces with the C₂H₆ and C₂H₄ was examined using in-situ DRIFT spectroscopy at 450°C, as shown in Fig. 9. Figures 9(a) and 9(c) show spectra collected in the presence of C₂H₆ and C₂H₄, respectively. The DRIFT spectra were acquired for 35 min, during which time the oxygen inserted into the CO₂ and CO species was solely derived from the lattice of the SFM perovskites. The molecular C₂H₆ is responsible for two strong peaks located at 2800–3100 cm⁻¹ and 1440 cm $^{-1}$, which were observed in the spectra [31]. The CO₂ peaks were detected at 2360 cm⁻¹ and 2330 cm⁻¹, while the CO peaks were observed at 2190 cm⁻¹ and 2100 cm⁻¹ [32]. The surface of SFM45 produced only CO2 as a product, while SFM40 and SFM35 produced both CO and CO2. Additionally, the infrared band for CH4 was observed at 1305 cm⁻¹ on SFM40 and SFM35 [32]. The results suggest that C-C bond cracking occurs on the surface of SFM perovskites when the Mo stoichiometry is below 0.45. However, the strong CH₄ peak at 3015 cm⁻¹ could not be distinguished as it overlaps with the strong C2H6 peak. To allow for a clear comparison of the deep oxidation towards CO2 among the SFM perovskites, the peak intensity ratio of CO2 (2365 cm-1) to

 C_2H_6 (2968 cm–1) was plotted as a function of time in Fig. 9(b). We observed that the oxidation of C_2H_6 to CO_2 occurred more rapidly on SFM perovskites with a lower Mo stoichiometry, with I_{CO2}/I_{C2H6} approaching 0.94 on SFM45, 1.01 on SFM40, and 1.13 on SFM35. This suggests that SFM perovskites with lower Mo stoichiometry are more likely to activate and oxidize C_2H_6 rapidly, as the high mobility of oxygen ions through the perovskite lattice allows for the increased production of CO_2 , resulting in the C_2H_4 selectivity being decreased.

In the field of ethane oxidative dehydrogenation (ODH), the catalytic activity for C_2H_4 activation is a crucial factor in determining C_2H_4 selectivity. This is because C_2H_4 is more reactive with oxygen. Therefore, an investigation on C_2H_4 conversion using in situ DRIFTS at 400° C was carried out on SFM perovskites (as shown in Fig. 9(c)). The IR peaks between 2800 cm^{-1} and 3300 cm^{-1} correspond to C_2H_4 and CO_2 peaks on the SFM perovskites, which increased over 35 min. The peak intensity ratio of CO_2 (2365 cm^{-1}) to C_2H_4 (2988 cm^{-1}) as a function of time is presented in Fig. 9(d). It was observed that I_{CO2}/I_{C2H6} on SFM35 approached 1.41, which is significantly higher than the ratio of 0.58 on SFM45. This indicates that SFM perovskites with a lower Mo content can easily activate and convert C_2H_4 to CO_2 , thereby reducing the C_2H_4

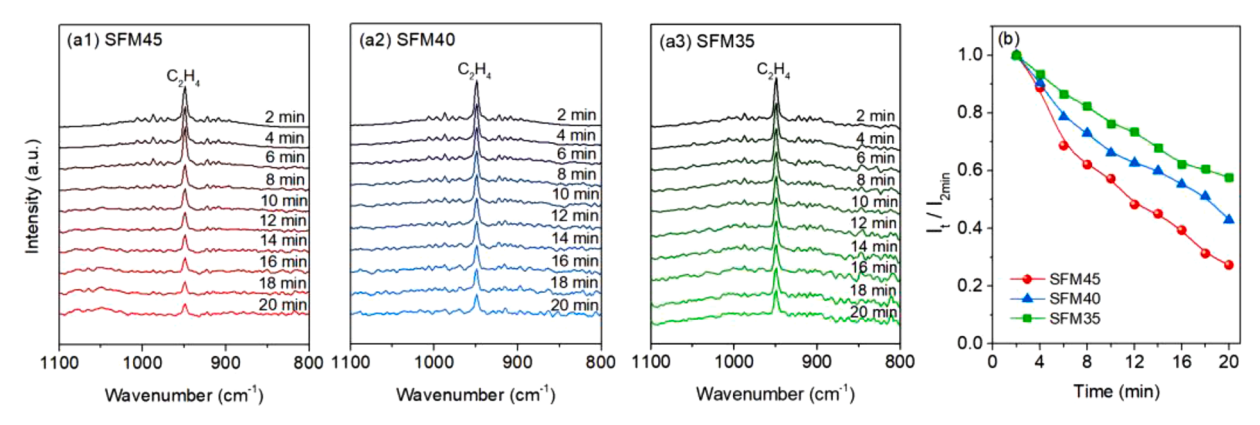


Fig. 10. (a) TPD-DRIFTS of C₂H₄ at 50 °C on SFM perovskites and (b) peak intensities of C₂H₄ (949.5 cm⁻¹) normalized by the peak at 2 min.

selectivity in ODHE.

Further investigation into the surface adsorption/desorption properties of SFM perovskites was conducted using DRIFTS to elucidate the basis for the selective conversion of C_2H_6 on SFM45 in comparison to SFM40 and SFM35. Powder samples were exposed to C_2H_4 at 50 °C and then, DRIFTS spectra were collected every 2 min under a helium flow of 30 ccm. As shown in Fig. 10(a), the intensity of C_2H_4 peak located at 949.5 cm $^{-1}$ gradually decreased with time on all samples. At 20 min, the peak intensity was the lowest for SFM45 and the highest for SFM35. Fig. 10(b) provides a clear comparison of the peak intensity normalized by the peak at 2 min (I_t / I_{2min}). I_t / I_{2min} approached 0.27 on SFM45 at 20 min, 0.43 on SFM40, and 0.57 on SFM35. The strong adsorption of C_2H_4 on the surface of catalysts increases the chance of C_2H_4 oxidation to CO and CO₂, resulting in a decreased selectivity for C_2H_4 in ODHE. Therefore, the ease of desorption of C_2H_4 on the SFM45 perovskite may partially account for the higher selectivity of C_2H_4 .

4. Conclusions

The present study investigated $Sr_2Fe_{2-x}Mo_xO_{6-\delta}$ (SFMx, x=0.35, 0.40, 0.45) double perovskites with different B-site stoichiometry as anodes for oxidative dehydrogenation of ethane (ODHE). XRD showed that the cubic crystal structure remained intact when the B-site stoichiometry was changed. The TPR analysis showed that the reducibility of SFM perovskites could be tuned by adjusting the ratio of Mo to Fe in the stoichiometry. Furthermore, the electrical conductivity of SFM perovskites was found to increase with decreasing Mo content due to the stronger Mo-O bonds than Fe-O bonds. The ODHE experiments in a SOEC using SFM perovskites as anode electrocatalysts indicated that the reaction was catalyzed application of electrical bias and the oxide ion flux to the anode surface. Among the different SFM perovskites with varying Mo content, SFM45 exhibited the highest conversion of C₂H₆ and selectivity toward C2H4. This result was attributed to its moderate oxygen mobility and its ability for fast desorption of C2H4. In-situ DRIFTS experiments under C₂H₆ and C₂H₄ provided further evidence that the oxygen ions provided by the lattice of perovskites were the key species involved in the activation of C2H6, and SFM perovskite with more Mo content suppressed the deep oxidation of C2H4 to carbon oxides. These findings provide valuable insights into the design and development of efficient anode electrocatalysts for ODHE.

CRediT authorship contribution statement

Jaesung Kim: Conceptualization, Investigation, Methodology, Data curation, Formal analysis, Writing – original draft. Matthew Ferree: Investigation, Formal analysis, Writing – review & editing. Seval Gunduz: Investigation, Formal analysis, Writing – review & editing. Anne C. Co: Formal analysis, Writing – review & editing. Umit S. Ozkan: Conceptualization, Funding acquisition, Project administration, Resources, Supervision, Formal analysis, Writing – review & editing.

Declaration of Competing Interest

The authors declare the following financial interests/personal relationships which may be considered as potential competing interests: Umit Ozkan reports financial support was provided by USDOE and NSF

Acknowledgement

We would like to gratefully acknowledge the financial support provided for this work by the U.S. Department of Energy, Office of Science, Office of Basic Energy Sciences under the Award Number DE-FG02-07ER15896 and the U.S. National Science Foundation, under the award number 1932638.

Reference

- [1] D. Noon, B. Zohour, S. Senkan, Oxidative coupling of methane with La₂O₃–CeO₂ nanofiber fabrics: A reaction engineering study, J. Nat. Gas Sci. Eng. 18 (2014) 406–411.
- [2] Y. Xiang, H. Wang, J. Cheng, J. Matsubu, Progress and prospects in catalytic ethane aromatization, Catal. Sci. Tech. 8 (2018) 1500–1516.
- [3] E.E. Stangland, Shale Gas Implications for C2-C3 Olefin Production: Incumbent and Future Technology, Annu. Rev. Chem. Biomol Eng 9 (2018) 341–364.
- [4] R. Koirala, R. Buechel, F. Krumeich, S.E. Pratsinis, A. Baiker, Oxidative Dehydrogenation of Ethane with CO2over Flame-Made Ga-Loaded TiO₂, ACS Catal 5 (2014) 690–702.
- [5] T. Ren, M. Patel, K. Blok, Olefins from conventional and heavy feedstocks: Energy use in steam cracking and alternative processes, Energy 31 (2006) 425–451.
- [6] S. Najari, S. Saeidi, P. Concepcion, D.D. Dionysiou, S.K. Bhargava, A.F. Lee, K. Wilson, Oxidative dehydrogenation of ethane: catalytic and mechanistic aspects and future trends. Chem. Soc. Rev. 50 (2021) 4564–4605.
- [7] X. Zhang, L. Ye, H. Li, F. Chen, K. Xie, Electrochemical Dehydrogenation of Ethane to Ethylene in a Solid Oxide Electrolyzer, ACS Catal 10 (2020) 3505–3513.
- [8] S. Liu, Y. Behnamian, K.T. Chuang, Q. Liu, J.-L. Luo, A-site deficient La_{0.2}Sr_{0.7}TiO_{3-δ} anode material for proton conducting ethane fuel cell to cogenerate ethylene and electricity, J. Power Sources 298 (2015) 23–29.
- [9] D. Dogu, K.E. Meyer, A. Fuller, S. Gunduz, D.J. Deka, N. Kramer, A.C. Co, U. S. Ozkan, Effect of lanthanum and chlorine doping on strontium titanates for the electrocatalytically-assisted oxidative dehydrogenation of ethane, Appl. Catal. B 227 (2018) 90–101.
- [10] L. dos Santos-Gómez, L. León-Reina, J.M. Porras-Vázquez, E.R. Losilla, D. Marrero-López, Chemical stability and compatibility of double perovskite anode materials for SOFCs, Solid State Ion 239 (2013) 1–7.
- [11] Q. Liu, X. Dong, G. Xiao, F. Zhao, F. Chen, A novel electrode material for symmetrical SOFCs, Adv. Mater. 22 (2010) 5478–5482.
- [12] M.K. Rath, K.-T. Lee, Superior electrochemical performance of non-precious Co-Ni-Mo alloy catalyst-impregnated Sr₂FeMoO₆₋₈ as an electrode material for symmetric solid oxide fuel cells, Electrochim. Acta 212 (2016) 678–685.
- [13] A. Vaitkus, A. Merkys, S. Grazulis, Validation of the Crystallography Open Database using the Crystallographic Information Framework, J. Appl. Crystallogr. 54 (2021) 661–672.
- [14] B.H. Toby, R.B. Von Dreele, GSAS-II: the genesis of a modern open-source all purpose crystallography software package, J. Appl. Crystallogr. 46 (2013) 544-549
- [15] K. Momma, F. Izumi, VESTA3 for three-dimensional visualization of crystal, volumetric and morphology data, J. Appl. Crystallogr. 44 (2011) 1272–1276.
- [16] D. Sanchez, C. Kozyrakis, ZSim: Fast and Accurate Microarchitectural Simulation of Thousand-Core Systems, ACM SIGARCH Computer architecture news 41 (2013) 475–486.
- [17] Y. Li, X. Chen, Y. Yang, Y. Jiang, C. Xia, Mixed-Conductor Sr₂Fe_{1.5}Mo_{0.5}O₆₋₈ as Robust Fuel Electrode for Pure CO₂ Reduction in Solid Oxide Electrolysis Cell, ACS Sustain. Chem. Eng. 5 (2017) 11403–11412.
- [18] U. Holzwarth, N. Gibson, The Scherrer equation versus the 'Debye-Scherrer equation, Nat. Nanotech. 6 (2011) 534.
- [19] C.A. Gärtner, A.C. vanVeen, J.A. Lercher, Oxidative Dehydrogenation of Ethane: Common Principles and Mechanistic Aspects, ChemCatChem 5 (2013) 3196–3217.
- [20] J. Feng, G. Yang, N. Dai, Z. Wang, W. Sun, D. Rooney, J. Qiao, K. Sun, Investigation into the effect of Fe-site substitution on the performance of Sr₂Fe_{1.5}Mo_{0.5}O_{6-δ} anodes for SOFCs, J. Mater. Chem. A 2 (2014) 17628–17634.
- [21] G. Miao, C. Yuan, T. Chen, Y. Zhou, W. Zhan, S. Wang, $Sr_2Fe_{1+x}Mo_{1-x}O_{6-\delta}$ as anode material of cathode–supported solid oxide fuel cells, Inter. J. Hydrog. Energy 41 (2016) 1104–1111.
- [22] L. Skutina, E. Filonova, D. Medvedev, A. Maignan, Undoped Sr₂MMoO₆ Double Perovskite Molybdates (M = Ni, Mg, Fe) as Promising Anode Materials for Solid Oxide Fuel Cells, Materials (Basel) 14 (2021) 1715.
- [23] M. Descostes, F. Mercier, N. Thromat, C. Beaucaire, M. Gautier-Soyer, Use of XPS in the determination of chemical environment and oxidation state of iron and sulfur samples: constitution of a data basis in binding energies for Fe and S reference compounds and applications to the evidence of surface species of an oxidized pyrite in a carbonate medium, Appl. Surf. Sci. 165 (2000) 288–302.
- [24] Y. Jiang, Y. Yang, C. Xia, H.J.M. Bouwmeester, Sr₂Fe_{1.4}Mn_{0.1}Mo_{0.5}O₆₋₈ perovskite cathode for highly efficient CO2 electrolysis, J. Mater. Chem. A 7 (2019) 22939–22949.
- [25] H. Chang, E. Bjørgum, O. Mihai, J. Yang, H.L. Lein, T. Grande, S. Raaen, Y.-A. Zhu, A. Holmen, D. Chen, Effects of Oxygen Mobility in La–Fe-Based Perovskites on the Catalytic Activity and Selectivity of Methane Oxidation, ACS Catal 10 (2020) 2707, 2710.
- [26] W.Y. Hernández, M.N. Tsampas, C. Zhao, A. Boreave, F. Bosselet, P. Vernoux, La/ Sr-based perovskites as soot oxidation catalysts for Gasoline Particulate Filters, Catal. Today 258 (2015) 525–534.
- [27] Z. Zhao, H. Dai, J. Deng, Y. Du, Y. Liu, L. Zhang, Three-dimensionally ordered macroporous La_{0.6}Sr_{0.4}FeO_{3—5}: High-efficiency catalysts for the oxidative removal of toluene, Microporous Mesoporous Mater 163 (2012) 131–139.
- [28] D.J. Deka, S. Gunduz, T. Fitzgerald, J.T. Miller, A.C. Co, U.S. Ozkan, Production of syngas with controllable H₂/CO ratio by high temperature co-electrolysis of CO₂ and H₂O over Ni and Co- doped lanthanum strontium ferrite perovskite cathodes, Appl. Catal. B 248 (2019) 487–503.
- [29] P. Kumar, N.K. Singh, A.S.K. Sinha, P. Singh, Structural and electrical characterizations of cerium (Ce3+)-doped double perovskite system Sr₂NiMoO_{6-δ}, Appl. Phys. A 122 (2016).

- [30] E. Hernández, F. Baiutti, A. Morata, M. Torrell, A. Tarancón, Infiltrated mesoporous oxygen electrodes for high temperature co-electrolysis of H₂O and CO₂ in solid oxide electrolysis cells, J. Mater. Chem. A 6 (2018) 9699–9707.
- [31] G. Karamullaoglu, T. Dogu, Oxidative dehydrogenation of ethane over a monolith coated by molybdenum-vanadium-niobium mixed-oxide catalyst, Chem. Eng. Commun. 190 (2010) 1427–1438.
- [32] J. Kim, Y.J. Kim, M. Ferree, S. Gunduz, A.C. Co, M. Kim, U.S. Ozkan, In-situ exsolution of bimetallic CoFe nanoparticles on (La,Sr)FeO₃ perovskite: Its effect on electrocatalytic oxidative coupling of methane, Appl. Catal. B 321 (2023), 122026.